

## Airborne ultrasonic transducer using polymer-based elastomer with high output-to-weight ratio

Jiang Wu\*, Yosuke Mizuno, Marie Tabaru, and Kentaro Nakamura

Precision and Intelligence Laboratory, Tokyo Institute of Technology, Yokohama 226-8503, Japan  
E-mail: wujiang@sonic.pi.titech.ac.jp

Received February 6, 2015; accepted May 19, 2015; published online July 2, 2015

With the properties of low density, low elastic modulus, and low mechanical loss, poly(phenylene sulfide) (PPS) is a suitable material as the elastomer in an airborne ultrasonic transducer for generating large vibration velocity. In this study, we design and fabricate a transducer composed of a PPS-based longitudinal vibrator and a PPS-based disk of 0.3 mm thickness to obtain high-intensity ultrasound. The rated sound pressure at a distance of 300 mm reached 38.9 Pa (125 dB, 0 dB re. 0.02 mPa) when the frequency and voltage were 58.90 kHz and 20 V. The weight of this transducer is 6.3 g. The ratio of the sound pressure to the weight of the prototype transducer is 1.8 times larger than that of the commercial transducer. The experimental results indicate that PPS is a good substitute for metal as the elastomer for manufacturing airborne ultrasonic transducers with a high output-to-weight ratio. © 2015 The Japan Society of Applied Physics

### 1. Introduction

Airborne ultrasonic transducers have been widely used in industry and daily life, for instance, in rat-repelling, deforming,<sup>1–3)</sup> deliquoring,<sup>4)</sup> and distance detection.<sup>5–10)</sup> Since its first invention, many optimizations have been carried out mainly on the structure of the transducers.<sup>2–4,11–19)</sup> Gallego-Juárez et al. attached a large plate on top of a Langevin vibrator and introduced a stepped structure in the plate to adjust the phase difference in the bending vibration.<sup>2–4)</sup> This transducer supplies a very intense sound pressure spot. However, the volume of the transducer is too large to change the radiation direction. On the other hand, for sensing and ranging applications, a small airborne ultrasonic transducer composed of an aluminum film cone and a bending vibrator has been widely used for a long time. Recently, 285 elements of such commercial transducers have been used to form a two-dimensional array. The controllable removal of liquid and the levitation of tiny polystyrene balls in a wide range have been demonstrated.<sup>20,21)</sup> For wider applications, a lightweight airborne ultrasonic transducer that can produce high intensity ultrasound is highly required. The adaption of some materials with low densities, low elastic moduli, and low mechanical loss is applicable for achieving high-intensity pressure and lightweight for the airborne ultrasonic transducer. With the recent development in material industry, a variety of new polymers have been invented and some of these industrial polymers were used as a matching layer and backing in MHz transducers for medical applications.<sup>14)</sup> In recent reports, one of the functional polymers, namely, poly(phenylene sulfide) (PPS), has been used as the vibrator in an ultrasonic motor.<sup>22–24)</sup> The most important property of the PPS-based vibrator for ultrasonic motor was the high vibration amplitude; and thus, it is expected that PPS is also prospective to be applied to an airborne ultrasonic transducer. In this study, using PPS as the elastomer, we design and fabricate a sandwich-shaped longitudinal transducer with a vibrating-disk film for ultrasound applications in air.

### 2. Materials and structure

The proposed airborne ultrasonic transducer is mainly composed of a bar-shaped longitudinal vibrator and a thin

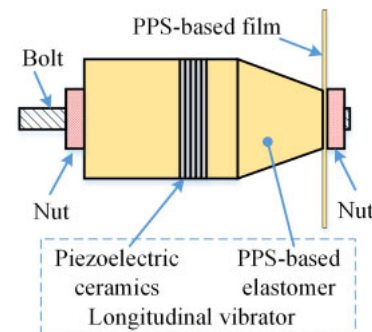
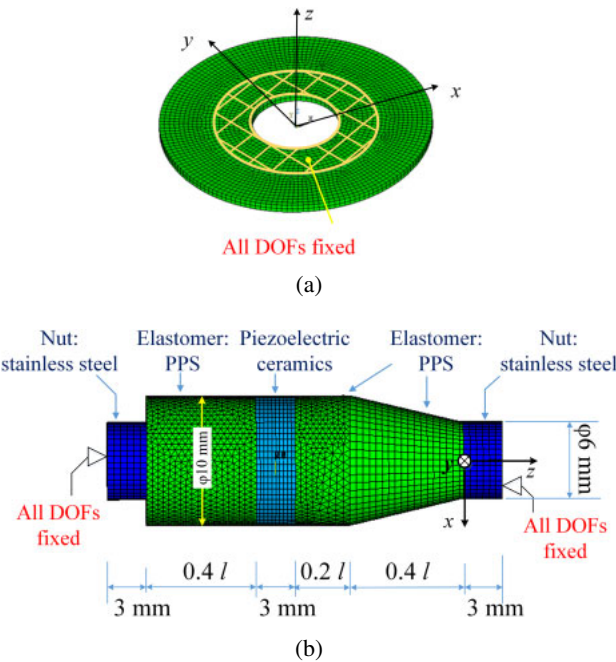


Fig. 1. (Color online) Structure of the airborne ultrasonic transducer.

Table I. Mechanical parameters of the tested PPS.

Density ( $10^3 \text{ kg/m}^3$ )	1.35
Elastic modulus (GPa)	3.45
Poisson's ratio	0.36

film, as shown in Fig. 1. Both the longitudinal vibrator and the thin film are made of PPS. As a new functional polymer, PPS has the properties of low elastic modulus, low density, and high mechanical quality factor,<sup>22,25–30)</sup> and some of the mechanical parameters of the PPS used in this study are shown in Table I. Five pieces of ring-shaped piezoelectric ceramics (Fuji Ceramics C213) are clamped in the middle of the PPS-based bar using a stainless steel bolt. The thin-film radiator is clamped on top of the longitudinal vibrator by a stainless steel nut. In this study, a nut with a flat surface is used to allow the film to come into full contact with the top of the longitudinal vibrator with a uniformly distributed pressure. The height and diameter of the nut are 4 and 6 mm, respectively. In conventional Langevin vibrators, both ends are under free condition and act as wave antinodes. However, in the longitudinal vibrator proposed in this paper, the displacements at both ends of the nuts are extremely small because the stiffness of the stainless steel bolt is much higher than that of the PPS-based elastomer. Thus, in the numerical simulation stated later, we used a simplified model, in which the ends of the nuts are fixed as an approximation.



**Fig. 2.** (Color online) Meshing models of (a) the PPS-based thin film and (b) the simplified meshing model of the longitudinal vibrator in modal analysis.

To generate high vibration velocity, the resonance frequencies of the longitudinal vibrator and the film should be identical. To find the appropriate vibration modes and dimensions, we calculated the resonance frequencies of the longitudinal vibrator and the thin film separately using the finite element method (FEM) software ANSYS (ver. 14.5). Figures 2(a) and 2(b) show the meshing models of the PPS-based thin film and the longitudinal vibrator, respectively. In Fig. 2(a), the nodes located within the 6-mm-diameter circle on the surface were set to be fixed in all degrees of freedom (DOFs), because this part on the thin film was clamped by a 6-mm-diameter nut. The resonance frequency of the PPS-based film is determined by the thickness and diameter. The resonance frequencies of different vibration modes were calculated and plotted as functions of the diameter from 10 to 15 mm with the thickness fixed at 0.3 mm. For the longitudinal vibrator depicted in Fig. 2(b), the resonance frequency is mainly determined by the length of the vibrator. Thus, we recorded the resonance frequencies of the longitudinal vibration modes when the length  $l$  was varied from 20 to 50 mm. The outer and inner diameters of the PPS-based bars were set to be 10 and 3.2 mm, respectively. Five pieces of piezoelectric ceramics with the outer and inner diameters of 10 and 4 mm were located between the PPS-based bars, and the total height of these piezoelectric ceramics was set to be 3 mm. In the calculation model, we used the simplified model with the fixed-fixed condition as explained before, and the outer surfaces of the nuts were restricted in all DOFs.

Figure 3 shows the simulation results of the resonance frequencies for the second longitudinal mode excited in the longitudinal vibrator and some bending modes in the thin film. For the longitudinal vibrator, the second longitudinal mode ( $L_2$ ) shows a higher efficiency than the other modes because the piezoelectric ceramics were set in the middle of the vibrator body. The simulation results of the resonance

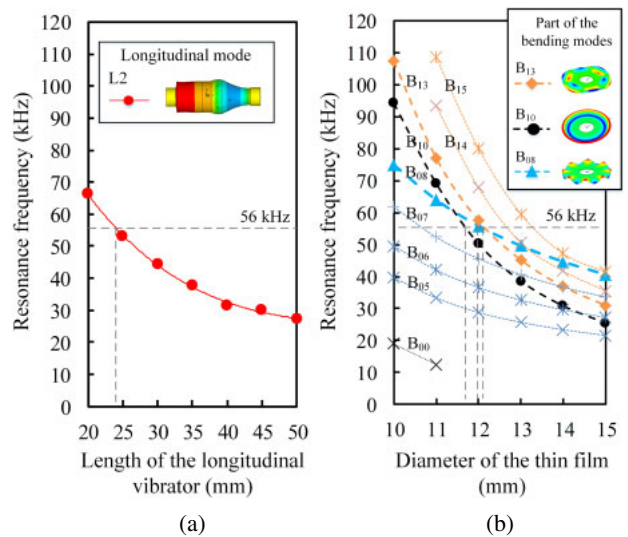


**Fig. 3.** (Color online) Simulation results of modal analysis: the resonance frequencies of (a) the longitudinal vibrator and (b) the thin film under different dimensions.

frequencies in the longitudinal vibrator as a function of length are shown in Fig. 3(a). To verify the effectiveness of the simplified model, we tested a complete model including the stainless steel bolt. The resonance frequencies calculated using the simplified model and complete model at 25 mm length were 53.173 and 54.271 kHz, respectively, which showed that the error is less than 2%. To reduce the calculation time, the simplified model is used for exploring the resonance frequencies in this study. For the thin film, among a number of vibration modes that can be generated, the appropriate mode should be selected carefully. In this paper, we paid attention to the sound pressure in free space generated by the different vibration modes. The resonance frequencies of the bending vibration modes are listed in Fig. 3(b). It is obvious that they can be categorized into three groups according to the deformation shapes. The sound pressure distribution generated in front of the vibrator is determined by the vibration distributions (modes) on the thin film. When the film is located at the  $xy$ -plane defined in Fig. 2, the sound pressure distributions  $p(x_0, y_0, z_0)$  for the typical modes of  $B_{10}$ ,  $B_{08}$ , and  $B_{13}$  are calculated using the formula:

$$p(x_0, y_0, z_0) = \frac{\rho}{2\pi} \iint_{S(x,y)} \frac{v(x, y)}{d(x, y)} \times \exp[-j \cdot k \cdot d(x, y)] dx dy \\ d(x, y) = \sqrt{(x_0 - x)^2 + (y_0 - y)^2 + z_0^2}, \quad (1)$$

where  $\rho$  is the density of air,  $k$  is the wave number, and  $d(x, y)$  is the distance between the observation position  $(x_0, y_0, z_0)$  and the element of the vibrating film located on  $(x, y, 0)$ . The center of the film is set at the origin of the coordinate system.  $v(x, y)$  is the vibration velocity distribution on the vibrating film, which is calculated using the harmonic analysis in ANSYS. Figure 4(a) shows the meshing model in harmonic analysis. Different from the models in modal analysis, the thin film was clamped on the  $xy$ -plane. The length of the longitudinal vibrator is set to be 24 mm and the diameter of the film is approximately 12 mm. A driving voltage of 20 V was applied on each piece of piezoelectric

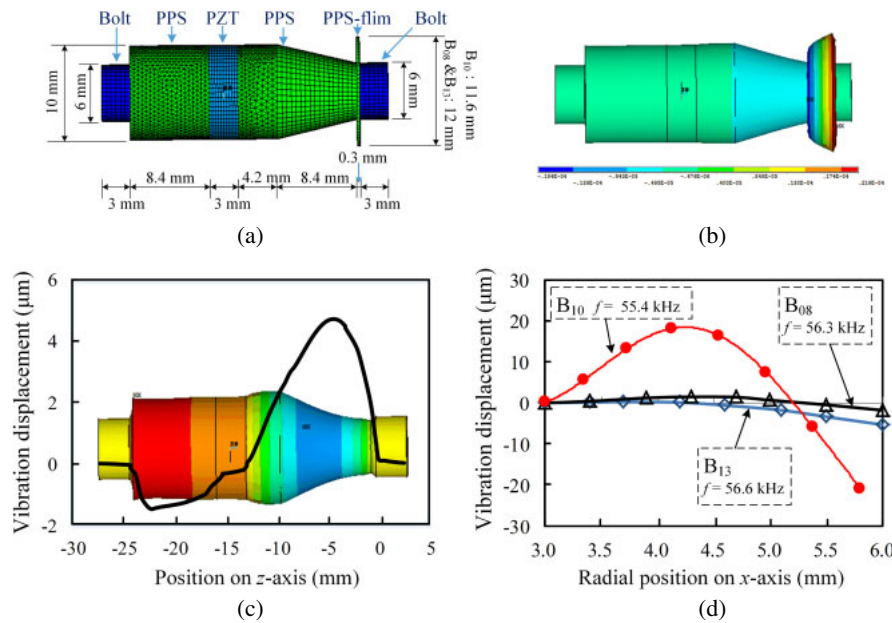


**Fig. 4.** (Color online) Simulation results of harmonic analysis: based on the model shown in (a), the vibration displacement is calculated and the deformation contour is shown in (b). The vibration displacements of the longitudinal transducer and the film are shown in (c) and (d), respectively.

ceramic as an excitation. Figure 4(b) shows the deformation contour at the frequency of 55.4 kHz. The vibration displacements of the longitudinal transducer and the thin film are shown in Figs. 4(c) and 4(d), respectively. The L<sub>2</sub> mode and B<sub>10</sub> mode were generated successfully on the longitudinal vibrator and thin film. The interface between the two parts acted as a node of the transducer as predicted. Substituting the vibration displacements of the film into Eq. (1), we obtained the sound pressure distributions in the xz-plane for the B<sub>10</sub>, B<sub>08</sub>, and B<sub>13</sub> modes, as shown in Fig. 5. In the B<sub>10</sub> mode, the main beams appear at 0 and  $\pm 45^\circ$  and the pressure of the central beam at a distance of 0.3 m in the z-axis reaches approximately 30 Pa. By contrast, with the B<sub>08</sub> and B<sub>13</sub> modes, sound beams do not appear in the z-direction and the sound pressures are extremely low. These are mainly caused by the low vibration velocities and the interference between the waves generated from the in-phase and out-of-phase vibrations along the circumference of the vibrating film in B<sub>08</sub> and B<sub>13</sub> modes. Based on the above analysis, we fabricate a prototype transducer with the L<sub>2</sub> and B<sub>10</sub> modes shown in Fig. 6(a) and measure the sound pressure in free space under different driving voltages. The dimensions of the prototype transducer are the same as those of the simulation model shown in Fig. 4(a).

### 3. Experimental results

The experimental setup shown in Fig. 6(b) was built to evaluate the prototype transducer. The transducer was fixed at the center of a rotating stage, and the angle  $\theta$  was changed by rotating the stage. A 1/8-in. microphone (ACO 7118) was used as a calibrated sound sensor. A sound absorption sponge was arranged to decrease the effects of reflection on the measured results. The transducer was fixed by inserting one end of the bolt into the foamed styrol. As the displacement of the bolt is small and the foamed styrol is soft, the vibration velocities are insensitive to the insert length of the bolt. This fixing method simplifies the assembly of the transducer.

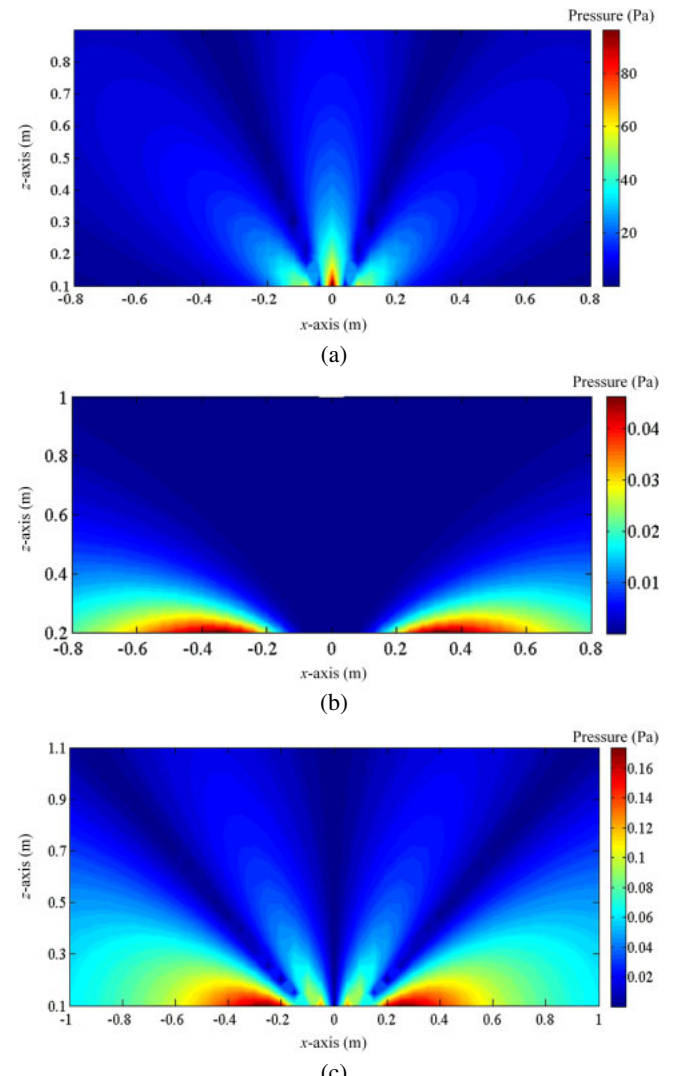


**Fig. 5.** (Color online) Simulation results: sound pressure distributions on xz-plane under (a) L<sub>2</sub>-B<sub>10</sub> mode, (b) L<sub>2</sub>-B<sub>08</sub> mode, and (c) L<sub>2</sub>-B<sub>13</sub> mode.

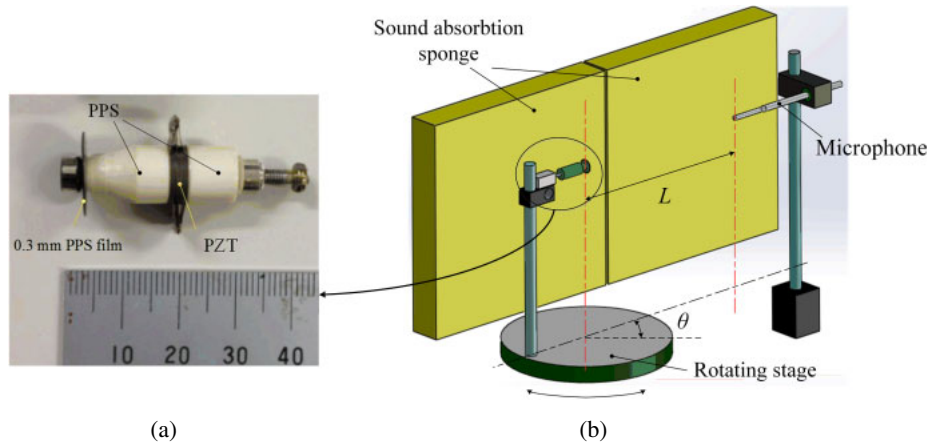


**Fig. 6.** (Color online) (a) Transducer prototype and (b) experimental setup.

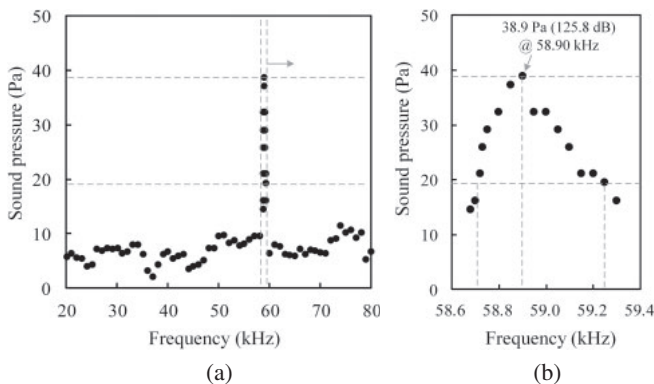


**Fig. 7.** Sound pressure as a function of driving frequency: (a) 20–80 kHz and (b) 58.6–59.4 kHz.

First, the working frequency for the prototype was determined. We measured the sound pressure, where the driving frequency was swept from 20 to 90 kHz at intervals of 1 kHz, while keeping the zero-to-peak voltage at 20 V. The distance  $L$  and the angle  $\theta$  were 300 mm and 0, respectively. The experimental results in Fig. 7(a) showed that a sharp peak appeared at the frequency of approximately 59 kHz. Detailed changes around 59 kHz were observed with a fine interval of 0.05 kHz. Figure 7(b) shows that the maximum sound pressure is up to 38.9 Pa (125.8 dB) at 58.90 kHz. The sound pressures are larger than 19.5 Pa for the frequency band from 58.70 to 59.25 kHz, which means that the  $-6$  dB bandwidth is 0.55 kHz. Figure 8 shows the vibration velocity distribution on the film at the driving frequency of 58.90 kHz, which was measured using a laser Doppler velocimeter (Polytec, NLV1232). It is clear that the vibration mode  $B_{10}$  was successfully generated.

Second, the dependences of the sound pressure on the rotating angle  $\theta$  and the distance  $L$  were measured for a driving frequency of 58.90 kHz and a voltage of 20 V. Figure 9 shows the directivity pattern at a distance of 300 mm. For the central beam, the sound pressure is larger than 19.5 Pa for the angle from  $-10$  to  $10^\circ$ . Comparing with the simulation results shown in Fig. 5, other than the main beams, two side lobes appear at the angles of  $\pm 65^\circ$ , which might be caused by the reflections by the bolt. Figure 10 shows the sound pressure as a function of the distance  $L$ . The pressure exceeds 100 Pa (134.0 dB) if the distance was less than 100 mm.

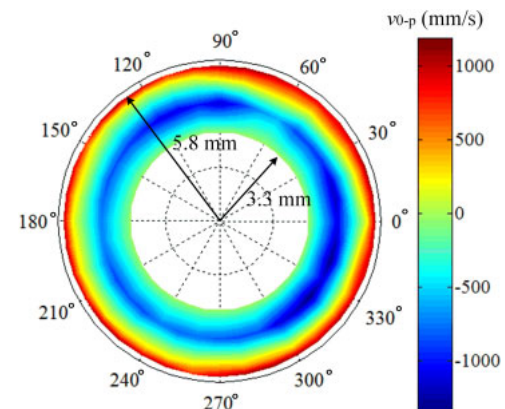


**Fig. 8.** (Color online) Vibration velocity distribution on PPS-based film measured with a laser Doppler velocimeter.

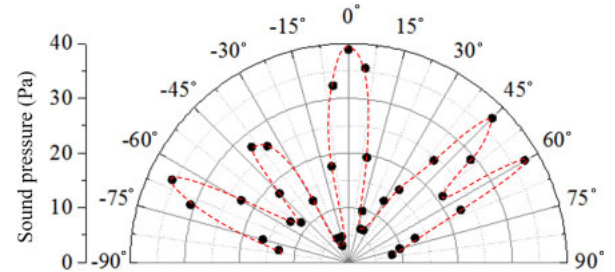


**Fig. 9.** (Color online) Directivity pattern measured at a distance of 300 mm.

Third, we investigated the dependence of the sound pressure on the driving voltage as shown in Fig. 11, where the frequency was approximately 59 kHz, and  $L$  and  $\theta$  were kept at 300 mm and 0. The driving frequency was adjusted every time the driving voltage was changed to obtain a higher sound pressure. The sound pressure approached 71.1 Pa (131.0 dB) under the zero-to-peak voltage of 40 V. When the driving voltage is lower than 40 V, the sound pressure linearly increases and the optimal frequency decreases, as the driving voltage increases.

Comparing with conventional transducers, the airborne ultrasonic transducer proposed in this paper has the features of higher sound pressure at rated voltage and higher output-to-weight ratio. The rated sound pressure of the typical

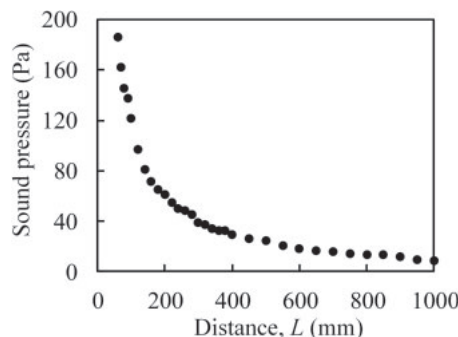


**Fig. 10.** Sound pressure as a function of the distance  $L$  between the transducer and the microphone.

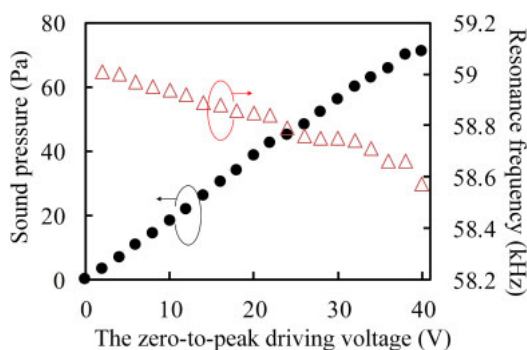


**Fig. 11.** (Color online) Sound pressure and resonance frequency as functions of driving voltage.

commercial ultrasonic transducer is 11.2 Pa (115 dB) when the maximum intensity of electric field in the piezoelectric ceramic is 47 V/mm, assuming that the thickness of the piezoelectric ceramic is 0.3 mm and the zero-to-peak voltage is 14.1 V. The sound pressure of the prototype transducer under the zero-to-peak voltage of 20 V, which was equivalent to the maximum intensity of the electric field of 40 V/mm, reached 38.9 Pa (125.8 dB). This value is 3.5 times higher than that of the commercial transducer. The weight of the prototype transducer is 6.3 g, 60% of which is that of the bolt and nuts made of stainless steel. The weight of the commercial transducer is approximately 3.2 g. Thus, the ratio of the sound pressure (output) to the weight of the prototype transducer is about 1.8 times larger than that of the conventional transducer. Furthermore, if the material with high elastic modulus and low density was used as the bolts, the weight of this transducer would be reduced. The experimental results indicate that PPS is a good substitute for metal as the elastomer in airborne ultrasonic transducers. The multiple-pole radiation pattern is another feature of this transducer. The angle coverage provided by the transducer with the multiple-pole radiation pattern is wider than that generated by the conventional one-main-pole type. In some applications, for instance, rat-repelling instruments and automobile radars, the numbers of transducers can be reduced if this new transducer is applied.

#### 4. Conclusions

To achieve higher sound pressure with minimum weight,

we designed and fabricated an airborne ultrasonic transducer using PPS as the elastomer, and measured the sound pressure distribution in free space. The experimental results showed that the sound pressure reached 38.9 Pa under the same intensity of electric field on the piezoelectric ceramics, which was 3.5 times as large as that of the commercial transducer. The ratio of the sound pressure to the weight of this transducer is 1.8 times larger than that of the commercial transducer. PPS, as a functional polymer with the properties of low density, low elastic modulus, and low mechanical loss, is expected to be applied in powerful and lightweight airborne ultrasonic transducers. In the future, we will integrate the polymer-based transducers to an array to obtain more powerful and controllable ultrasounds.

#### Acknowledgment

The authors thank Daicel Corporation for providing some of the polymer samples tested in the experiments.

- 1) J. A. Gallego-Juárez, *Phys. Procedia* **3**, 35 (2010).
- 2) J. A. Gallego-Juárez, *J. Sound Vib.* **26**, 411 (1973).
- 3) J. A. Gallego-Juárez, G. Rodriguez-Corral, and L. Gaete-Garreton, *Ultrasonics* **16**, 267 (1978).
- 4) J. A. Gallego-Juárez, L. Elvira-Segura, and G. Rodríguez-Corral, *Ultrasonics* **41**, 255 (2003).
- 5) A. Carullo and M. Parvis, *IEEE Sens. J.* **1**, 143 (2001).
- 6) H. Y. Jeon, H. Zhu, R. Derksen, E. Ozkan, and C. Krause, *Comput. Electron. Agric.* **75**, 213 (2011).
- 7) A. Hernandez, J. Urena, J. J. Garcia, M. Mazo, D. Hernanz, J. P. Derutin, and J. Serot, *IEEE Trans. Ultrason. Ferroelectr. Freq. Control* **51**, 1660 (2004).
- 8) D. Caicedo and A. Pandharipande, *IEEE Sens. J.* **12**, 849 (2012).
- 9) G. Andria, F. Attivissimo, and N. Giaquinto, *Measurement* **30**, 105 (2001).
- 10) S. Hirata and M. Kurosawa, *Ultrasonics* **52**, 873 (2012).
- 11) H. Okada, M. Kurosawa, S. Ueha, and M. Masuda, *Jpn. J. Appl. Phys.* **33**, 3040 (1994).
- 12) W. Manthey, N. Kroemer, and V. Magorl, *Meas. Sci. Technol.* **3**, 249 (1992).
- 13) L.-F. Ge, *IEEE Trans. Ultrason. Ferroelectr. Freq. Control* **46**, 1120 (1999).
- 14) K. Suzuki, K. Higuchi, and H. Tanigawa, *IEEE Trans. Ultrason. Ferroelectr. Freq. Control* **36**, 620 (1989).
- 15) C. Lee, W. Chuang, S. Lin, W. Wu, and C. Lin, *Jpn. J. Appl. Phys.* **52**, 05DA08 (2013).
- 16) A. Decharat, S. Wagle, and F. Melandso, *Jpn. J. Appl. Phys.* **53**, 05HB16 (2014).
- 17) T. Inoue and M. Kobayashi, *Jpn. J. Appl. Phys.* **53**, 07KC11 (2014).
- 18) M. Nakazawa, M. Tabaru, T. Aoyagi, K. Nakamura, and S. Ueha, *IEEE Trans. Ultrason. Ferroelectr. Freq. Control* **60**, 2175 (2013).
- 19) J. Kim, J. Jung, M. Kim, and K. Ha, *Jpn. J. Appl. Phys.* **53**, 07KF14 (2014).
- 20) T. Hoshi, M. Takahashi, T. Iwamoto, and H. Shinoda, *IEEE Trans. Haptics* **3**, 155 (2010).
- 21) T. Hoshi, Y. Ochiai, and J. Rekimoto, *Jpn. J. Appl. Phys.* **53**, 07KE07 (2014).
- 22) J. Wu, Y. Mizuno, K. Nakamura, S. Kambara, N. Okuyama, and K. Shimizu, *Proc. IEEE Int. Ultrasonics Symp.*, 2014, p. 2514.
- 23) J. Wu, Y. Mizuno, M. Tabaru, and K. Nakamura, Ext. Abstr. 75th Autumn Meet. Japan Society of Applied Physics, 2014, 18p-A15-10.
- 24) J. Wu, Y. Mizuno, M. Tabaru, and K. Nakamura, Proc. 35th Symp. Ultrasonic Electronics, 2014, p. 199.
- 25) W. Tantpanichakoon, M. Hata, K. Nitta, M. Furuuchi, and Y. Otani, *Polym. Degrad. Stabil.* **91**, 2614 (2006).
- 26) H. Hill and D. Brady, *Polym. Eng. Sci.* **16**, 831 (1976).
- 27) H. Zeng and K. Mai, *Macromol. Chem. Phys.* **187**, 1787 (1986).
- 28) R. J. Pace and A. Datyner, *J. Polym. Sci., Part B* **17**, 437 (1979).
- 29) M. Day and D. Budgell, *Thermochim. Acta* **203**, 465 (1992).
- 30) J. Scobbo, Jr., *Polym. Test.* **10**, 279 (1991).